

Room-temperature antiferromagnetic memory resistor

X. Marti^{1,2,3*}, I. Fina^{4,5}, C. Frontera⁴, Jian Liu⁶, P. Wadley^{3,7}, Q. He⁸, R. J. Paull¹, J. D. Clarkson¹, J. Kudrnovský⁹, I. Turek^{2,10}, J. Kuneš³, D. Yi⁶, J-H. Chu⁶, C. T. Nelson¹¹, L. You¹², E. Arenholz⁸, S. Salahuddin¹², J. Fontcuberta⁴, T. Jungwirth^{3,7} and R. Ramesh^{1,6}

The bistability of ordered spin states in ferromagnets provides the basis for magnetic memory functionality. The latest generation of magnetic random access memories rely on an efficient approach in which magnetic fields are replaced by electrical means for writing and reading the information in ferromagnets. This concept may eventually reduce the sensitivity of ferromagnets to magnetic field perturbations to being a weakness for data retention and the ferromagnetic stray fields to an obstacle for high-density memory integration. Here we report a room-temperature bistable antiferromagnetic (AFM) memory that produces negligible stray fields and is insensitive to strong magnetic fields. We use a resistor made of a FeRh AFM, which orders ferromagnetically roughly 100 K above room temperature, and therefore allows us to set different collective directions for the Fe moments by applied magnetic field. On cooling to room temperature, AFM order sets in with the direction of the AFM moments predetermined by the field and moment direction in the high-temperature ferromagnetic state. For electrical reading, we use an AFM analogue of the anisotropic magnetoresistance. Our microscopic theory modelling confirms that this archetypal spintronic effect, discovered more than 150 years ago in ferromagnets, is also present in AFMs. Our work demonstrates the feasibility of fabricating room-temperature spintronic memories with AFMs, which in turn expands the base of available magnetic materials for devices with properties that cannot be achieved with ferromagnets.

The energy barrier separating the two stable directions of ordered spins in ferromagnets is partly due to the macroscopic moment and the dipolar shape anisotropy fields present in the sample. Another contribution is provided by the magnetocrystalline anisotropy energy arising from spin-orbit coupling. As the relativistic spin-orbit coupling does not distinguish between ferromagnets and AFMs and magnetocrystalline anisotropies are even in the microscopic moment direction, such a bistability can be readily present even if the collective spin order is AFM (refs 1,2).

The magnetotransport counterparts of the relativistic energy anisotropies are the anisotropic magnetoresistance (AMR) effects^{3,4}. Their presence in AFMs was predicted⁵ and experimentally confirmed^{6–10} in tunnel junction devices with an AFM IrMn electrode and a non-magnetic counter-electrode on the other side of the tunnel barrier. The spin axis of AFM-aligned moments can point in different directions and can be detected electrically by the AMR as in ferromagnets.

Owing to the net moment in ferromagnetic materials, the electron spins can be oriented by a magnetic field larger than the coercive field, whose strength is limited by the magnetic anisotropy fields and rarely exceeds ~1 T. Compensated AFMs, in contrast, have zero net magnetization and thus, unlike ferromagnets, produce no stray magnetic fields. The zero magnetization also implies that AFMs are much less sensitive to external magnetic fields than

ferromagnets. The sensitivity scale of AFMs is set by the ~100 T exchange fields¹¹.

Recently, the concept of an AFM memory was explored on an atomic scale¹². Bistable AFM configurations of a few Fe atom chains were detected using low-temperature, atomically resolved measurement by a spin-polarized tip of a scanning tunnelling microscope. Here we demonstrate an AFM-AMR memory that has a simple ohmic resistor geometry and whose magnetic state can be stored and detected at room temperature. We show that it is insensitive to magnetic fields and produces negligible stray magnetic fields. In the first part of the paper, we summarize key experimental results demonstrating the writing, reading and retention functionalities of our AFM memory and present microscopic discussion and calculations of the AFM-AMR phenomenon. In the second part we report structural characterization of our FeRh samples and provide a more detailed discussion of the magnetic and magnetotransport properties measured over a broad field and temperature range covering both the AFM and ferromagnetic states.

Demonstration of the AFM memory resistor concept

Our main results are summarized in Fig. 1. We have grown a 100-nm-thick, single-crystalline film of the FeRh AFM (refs 13–15) on a cubic MgO substrate. The AFM–ferromagnetic transition occurs in

¹Department of Materials Science and Engineering and Department of Physics, University of California, Berkeley, California 94720, USA, ²Department of Condensed Matter Physics, Faculty of Mathematics and Physics, Charles University, 12116 Praha 2, Czech Republic, ³Institute of Physics ASCR, v.v.i., Cukrovarnická 10, 162 53 Praha 6, Czech Republic, ⁴Institut de Ciència de Materials de Barcelona, ICMAB-CSIC, Campus UAB, Bellaterra E-08193, Spain, ⁵Max Planck Institute of Microstructure Physics, Weinberg 2, Halle D-06120, Germany, ⁶Materials Science Division, Lawrence Berkeley National Laboratory, Berkeley, California 94720, USA, ⁷School of Physics and Astronomy, University of Nottingham, Nottingham NG7 2RD, UK, ⁸Advanced Light Source, Lawrence Berkeley National Laboratory, Berkeley, California 94720, USA, ⁹Institute of Physics ASCR, v.v.i., Na Slovance 2, 182 21 Praha 8, Czech Republic, ¹⁰Institute of Physics of Materials ASCR, v.v.i., Žitkova 22, Brno 616 62, Czech Republic, ¹¹National Center for Electron Microscopy, Lawrence Berkeley National Laboratory, Berkeley, California 94720, USA, ¹²Department of Electrical Engineering and Computer Sciences, University of California, Berkeley, Berkeley, California 94720, USA. *email: xavi.marti@igsresearch.com

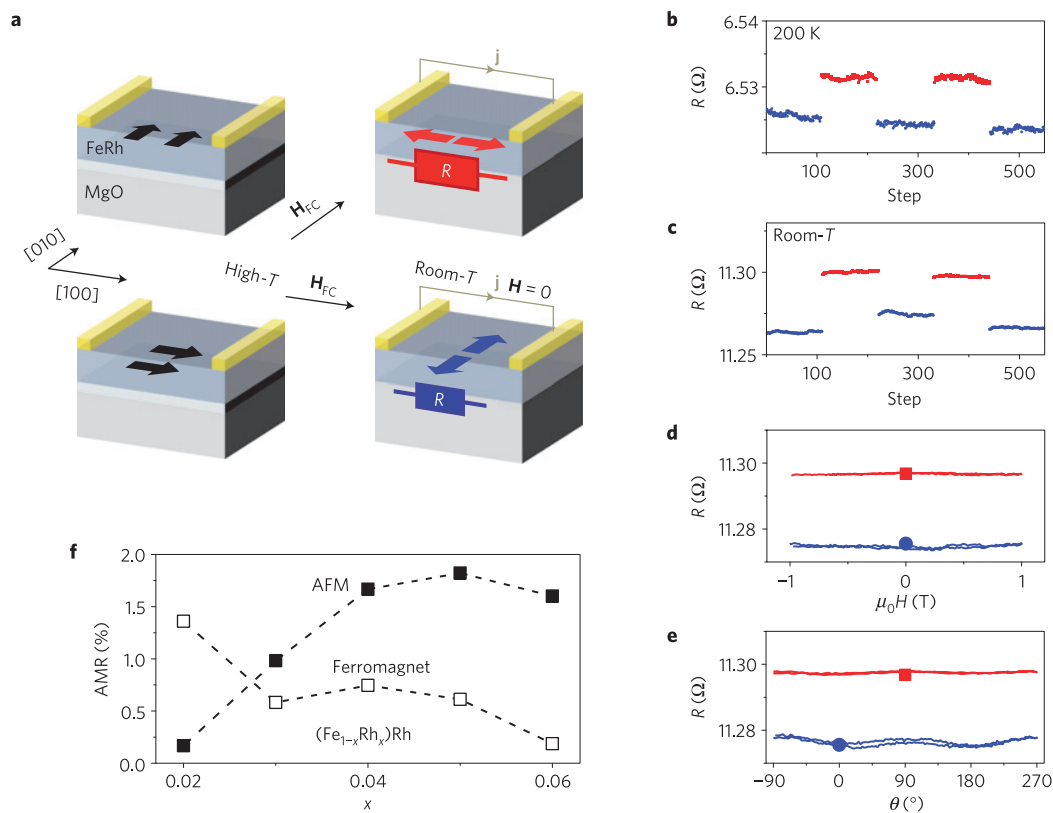


Figure 1 | AFM-AMR memory functionality in a FeRh resistor. **a**, Schematic illustration of the AFM FeRh/MgO structure and of the memory writing and reading set-up. For writing, the sample is cooled in a field H_{FC} from a temperature above the AFM-ferromagnetic transition in FeRh (we used maximum field of 9 T and temperature of 400 K allowed in our transport measurement set-up) to below the transition temperature (200 K). Black arrows denote the orientation of the magnetic moments in the ferromagnetic phase whereas either red or blue arrows denote two distinct configurations of the magnetic moments in the AFM phase. The resulting AFM spin axis in the low-temperature memory state depends on the direction of H_{FC} , which is either along the [100] or [010] crystal axis. For reading, electrical current j is driven between electrical contacts (yellow bars) along the [100] direction and the resistance is detected. **b**, Resistance measured at 200 K and zero magnetic field after field-cooling the sample with H_{FC} parallel (blue) and perpendicular (red) to the current direction. The two resistance states are clearly distinct and many successive measurement steps demonstrate the stability of the distinct memory states. **c**, The same as in **b**, but at room temperature. **d**, Stability of the two memory states at room temperature tested by measuring the resistance while sweeping a magnetic field H between ± 1 T applied along the [100] direction. **e**, The same as in **d**, while rotating a 1 T magnetic field. **f**, AMR values calculated for the Rh-rich $(Fe_{1-x}Rh_x)Rh$ random alloy using the Kubo formula CPA-TB-LMTO formalism. The AMR is defined as a relative difference between the resistivity for the spin axis parallel and perpendicular to the current, $AMR = (R_{s||j} - R_{s\perp j})/R_{s||j}$. Results are shown for the AFM ground state (filled symbols) and for a hypothetical zero-temperature ferromagnetic state (open symbols) of FeRh.

FeRh close to 400 K; at this temperature, we have applied a magnetic field H_{FC} to align its magnetization and the corresponding magnetic moments of FM FeRh along the applied magnetic field. The sample is then field-cooled below room temperature (200 K) and H_{FC} is then removed. In this AFM state with no applied magnetic field we perform a series of four-probe resistance measurements with the current j applied along the [100] substrate crystal direction. The same protocol is repeated several times with H_{FC} applied during field-cooling either along the [100] or [010] substrate crystal directions (Fig. 1a). The resulting resistances in the AFM state are stable and fully reproducible in the successive write-read cycles, and the two cooling-field directions define two distinct resistance states of the AFM. They remain distinct not only on removing the magnetic field but also when warming the AFM up to room temperature, as shown in Fig. 1b,c.

In Fig. 1d,e we demonstrate that the two AFM memory states are robust against strong magnetic field perturbations. After preparing one of the states by the above cooling-in-field procedure, we rotate the sample at room temperature in a magnetic field H of 1 T and observe a negligible effect on the resistance in either of the two AFM memory states (Fig. 1e). As in the rotation experiment, the

states are not disturbed by sweeping the magnitude of H at a fixed applied field angle (Fig. 1d). In the detailed discussion below we show that the retention in our AFM memory is not disturbed up to the highest fields (9 T) available in our transport measurement set-up. However, before resuming the detailed experimental analysis, we focus in the following paragraphs on the microscopic physics behind the observed distinct resistance states in our FeRh AFM.

Theory of the AFM-AMR

In this theoretical section, we first recall the fundamentals of the AMR relevant to our experiments and then discuss our quantitative modelling of the effect based on a relativistic density-functional transport theory^{16–20}. As already mentioned in the introduction, conceptually the AMR phenomena are equally present in AFMs as in ferromagnets. As AMR is an even function of the microscopic magnetic moment vector, it is the direction of the spin axis (s) rather than the direction of the macroscopic magnetization (M) relative to the current direction that primarily determines the effect. In collinear ferromagnets the two directions are equivalent. For the staggered spin configuration of compensated AFMs only the spin axis can be defined while the macroscopic magnetization is zero.

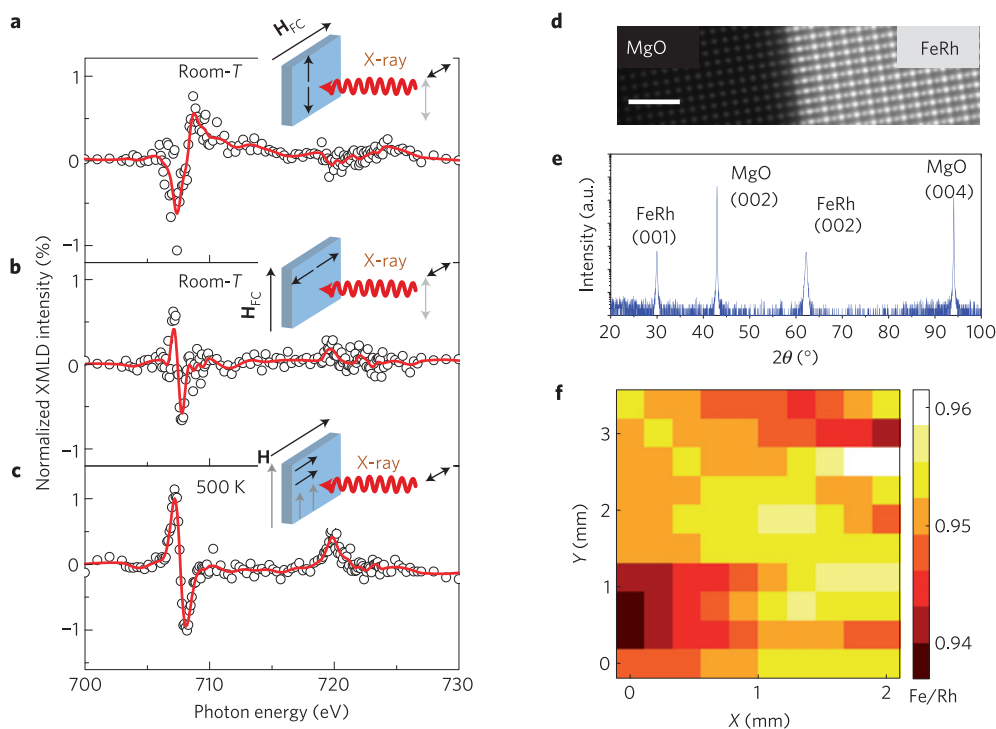


Figure 2 | Characterization of the magnetic and crystal structure of the FeRh film. **a**, Fe L-edge XMLD difference in absorption intensities in the AFM state of FeRh for the cooling-field vector $\mathbf{H}_{FC} \parallel [100]$ and the X-ray linear polarization vectors $\mathbf{E} \parallel [100]$ and $\mathbf{E} \parallel [010]$. **b**, The same as in **a**, for the cooling-field vector $\mathbf{H}_{FC} \parallel [010]$ and the X-ray linear polarization vectors $\mathbf{E} \parallel [100]$ and $\mathbf{E} \parallel [010]$. In **a, b**, the maximum field of 0.5 T allowed in the XMLD set-up was applied when cooling the sample from 500 to 200 K and then removed before room-temperature XMLD measurements were performed. **c**, Fe L-edge XMLD difference in absorption intensities in the ferromagnetic state of FeRh at 500 K for the X-ray linear polarization vector $\mathbf{E} \parallel [100]$ and applied magnetic fields $\mathbf{H} \parallel [100]$ and $\mathbf{H} \parallel [010]$. The AFM and ferromagnetic XMLD signals are of comparable strength and the signs of the signals are consistent with the AFM spin axis oriented perpendicular to \mathbf{H}_{FC} , as indicated in the insets. **d**, Cross-section image of the FeRh thin film at the interface with the MgO substrate, viewed down the the (112) and (100) zone axis of the two respective materials. Scale bar, 2 nm. **e**, θ - 2θ scan showing textured films; indicated are the (001) reflections of the substrate and the film. **f**, Compositional map of the Fe/Rh content of the film.

To date, studies of AMR phenomena in AFMs have focused on tunnelling devices^{5–10}. In analogy to the tunnelling AMR in ferromagnets^{21–26}, the origin of the phenomenon is ascribed to the changes in the equilibrium relativistic electronic structure (density of states) induced by rotating the spin axis with respect to crystal axes⁵. A recently reported AMR in an ohmic device fabricated from an AFM Sr_2IrO_4 film shares the anisotropic electronic structure origin of the tunnelling AMR (ref. 27). In the Sr_2IrO_4 AMR experiment, the current was driven through the film in the direction perpendicular to the sample plane while the AFM spin axis was rotated in the plane. This experimental geometry in which the angle between the spin axis and current is fixed and the resistance depends on the angle between the spin axis and crystal axes is referred to as the ‘crystalline’ ohmic AMR (refs 4,28). For both the tunnelling AMR and the crystalline ohmic AMR, the quantitative relativistic transport theory would require the combination of the calculated density of states anisotropy with the tunnelling or scattering matrix elements, respectively. As a proper modelling of these matrix elements for realistic sample parameters is in general a difficult problem, the theories have focused primarily on assessing the qualitative origin of these AMR phenomena based on the density of states anisotropy calculations.

In our ohmic FeRh resistor the different directions of the AFM spin axis are set by a field-cooling procedure in which the magnetic field is applied either along the [100] or [010] crystal axis of our MgO/FeRh sample. Owing to the in-plane cubic symmetry of the structure, the equilibrium density of states of the FeRh film is identical for the AFM spin axis set by the cooling field applied along

equivalent cubic axes. Unlike the above tunnelling or crystalline ohmic AMR, the equilibrium density of states anisotropy is not the origin of the resistance anisotropy we observe in our FeRh resistor. Instead, the effect originates from the change of the angle of the spin axis with respect to the electrical current direction. This is akin to the common ‘non-crystalline’ AMR in ferromagnets^{4,28}, which is the only component contributing to the AMR in polycrystalline samples or when the spin axis alternates between equivalent symmetry axes of the crystal. The dependence on the relative angle of the spin axis and current is the phenomenon that Kelvin detected in his more than 150-year-old seminal work on the AMR in Fe and Ni (ref. 3).

As the equilibrium density of states anisotropy of a clean crystal does not provide even a qualitative proxy to the non-crystalline AMR, its modelling remains a challenge despite the long history of the effect and the simple experimental geometry used for its detection. To first order, the non-crystalline AMR reflects the dependence of the scattering matrix elements of electrons, with momentum parallel to current, on the angle between the spin axis and the momentum. The spin dependence of the momentum scattering is due to the relativistic spin–orbit coupling. A quantitative modelling approach requires the identification of the dominant scattering mechanism and the use of a full quantum transport theory framework. In ferromagnets, such a quantitative description has been successfully applied to random metal alloys in which scattering is dominated by the alloy disorder and the relativistic band structure is reliably obtained using the density-functional theory^{16–20}. Here we apply an analogous formalism to calculate the non-crystalline ohmic AMR in our FeRh AFM.

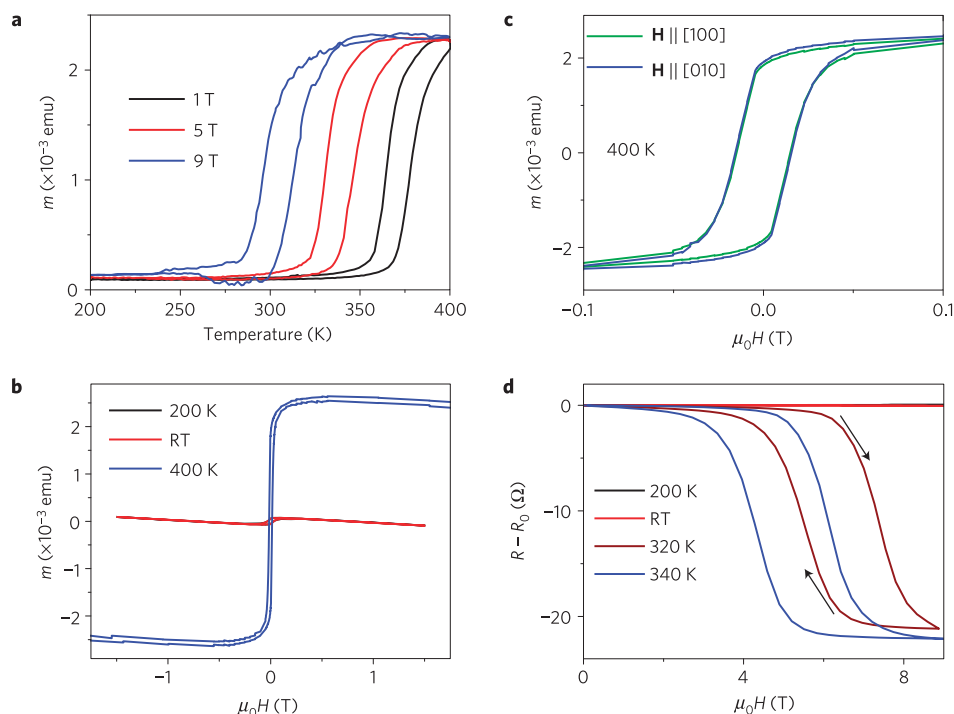


Figure 3 | Magnetic properties. **a**, Temperature dependence of the magnetization at 1, 5 and 9 T applied magnetic fields. **b**, Magnetic field dependence of the magnetization at 200 K, room-temperature and 400 K. **c**, Comparison of 400 K magnetization loops for magnetic field applied along the [100] and [010] MgO crystallographic directions. **d**, Magnetic field dependence of the resistance at 200 K, room-temperature, 320 and 340 K. Black arrows indicate the direction of the temperature sweep.

Results of our microscopic calculations are presented in Fig. 1f. We employed the relativistic, tight-binding linear muffin-tin orbital (TB-LMTO) density-functional theory of the band structure, the Kubo formula description of transport, and the alloy disorder is accounted for within the coherent potential approximation^{19,20} (CPA). The AMR plotted in Fig. 1f is defined as a relative difference between the resistivity for the spin axis parallel and perpendicular to the current, $\text{AMR} = (R_{s\parallel j} - R_{s\perp j})/R_{s\parallel j}$. This applies to both the AFM ground state of FeRh and a hypothetical zero-temperature ferromagnetic state that we also consider in our calculations for comparison. Following the chemical composition measurements shown below in Fig. 2, we assume in the calculations a Rh-rich ($\text{Fe}_{1-x}\text{Rh}_x$)Rh random alloy and calculate the AMR as a function of x . The experimentally determined non-stoichiometry in our samples corresponds to $x \approx 0.02\text{--}0.03$ ($\text{Fe}/\text{Rh} \sim 0.94\text{--}0.96$). For these values, the calculated AMR $\approx 0.1\text{--}1\%$ in the AFM state is in good agreement with the measured difference between the two resistance states (see also the temperature-dependent AFM-AMR measurements below). To confirm the robustness of the theoretically predicted AMR in AFMs we also performed control calculations for FeRh in which disorder- and temperature-dependent scattering (through phonons or magnons) is effectively modelled by a finite quasiparticle broadening of the Fermi level states. For resistivities similar to the experimental values, we consistently obtain AFM-AMR values close to a half of a per cent. The comparison of our calculated FeRh AMRs in the AFM ground state and the hypothetical zero-temperature ferromagnetic state highlights the expected equal presence and comparable magnitude of the AMR phenomena in these two distinct ordered spin states. Note that the calculated AFM-AMR even exceeds the ferromagnetic-AMR at stronger alloy disorder (larger x), as seen in Fig. 1f.

Important evidence is drawn from the calculated sign of the AFM-AMR in our FeRh sample. Similar to the calculated sign of

the AMR in the ferromagnetic state of FeRh and to the AMR sign in common transition-metal ferromagnets^{4,16–20}, our theory predicts a lower resistivity state for the AFM spin axis aligned perpendicular to the current. This confirms the scenario, anticipated in Fig. 1a, by which the field-cooling procedure sets in the spin-axis direction in the FeRh AFM state. In agreement with the theoretical sign of the AFM-AMR, the ferromagnetically aligned moments along the applied magnetic field H_{FC} at the high temperature rotate clockwise in one spin sublattice and anticlockwise in the other sublattice of FeRh until they reach the AFM configuration at the low temperature with the spin axis oriented perpendicular to H_{FC} .

X-ray magnetic linear dichroism

Further evidence for the above field-cooling writing scenario is provided by our Fe L-edge X-ray magnetic linear dichroism (XMLD) experiments. Using X-rays offers the elemental specificity while the magnetic linear dichroism, characterized by different absorption of light with its linear polarization vector \mathbf{E} oriented parallel or perpendicular to the spin axis, represents the optical analogue to the AMR (ref. 29). XMLD is also an even function of the microscopic magnetic moment vector and is equally present in AFMs as in ferromagnets²⁹. After field-cooling the sample from above the AFM–ferromagnetic transition down to 200 K and removing H_{FC} , we warmed the sample to room temperature and performed the XMLD measurements in the AFM state of FeRh. In Fig. 2a we plot the XMLD spectrum for the cooling-field vector $\mathbf{H}_{\text{FC}} \parallel [100]$ and the X-ray polarization vectors $\mathbf{E} \parallel [100]$ and $\mathbf{E} \parallel [010]$ ($I_{\mathbf{E}\parallel[100]} - I_{\mathbf{E}\parallel[010]}$). In Fig. 2b the X-ray polarization vector directions were set in the same order as in Fig. 2a; however, \mathbf{H}_{FC} was applied along the [010] axis. The opposite sign of the XMLD spectra in Fig. 2a,b confirms the magnetic origin of the linear dichroism signal and confirms that the AFM spin axes in the two field-cooling experiments are rotated by 90° with respect to each

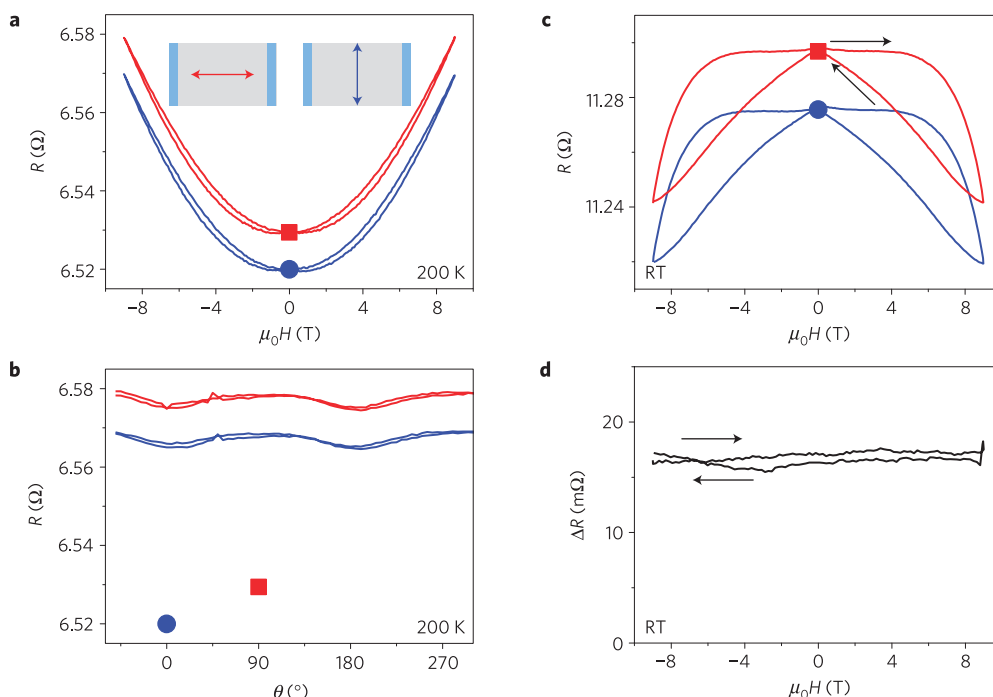


Figure 4 | Stability of the memory states at high magnetic fields. **a**, Resistance of the two memory states at 200 K and in a magnetic field swept between ± 9 T along the [100] direction. The insets show two distinct configurations of the AFM moments in the device. **b**, The same as in **a**, in a 9 T rotating magnetic field. In **a, b**, the red square and blue circle indicate the zero-field resistances of the two memory states after the cooling-in-field writing procedure. **c**, The same as in **a**, measured at room temperature. **d**, The difference between resistances of the two memory states plotted in **c**. In **c, d**, the arrows indicate the direction of sweeping of the magnetic field.

other. To determine the spin-axis orientation, in Fig. 2c we plot the Fe L-edge XMLD spectrum in the high-temperature ferromagnetic state of FeRh. The measurement was performed with $\mathbf{E} \parallel [100]$ and in applied magnetic fields $\mathbf{H} \parallel [100]$ and $\mathbf{H} \parallel [010]$ ($I_{\mathbf{H} \parallel [100]} - I_{\mathbf{H} \parallel [010]}$). The ferromagnetic XMLD signal has a similar shape but an opposite sign to the XMLD ($I_{\mathbf{E} \parallel [100]} - I_{\mathbf{E} \parallel [010]}$) in the AFM state with $\mathbf{H}_{\text{FC}} \parallel [100]$ (Fig. 2a). As the moment/spin axis is parallel to the field in the ferromagnetic state, this sign change indicates that the AFM spin axis is along [010], confirming the expected AFM spin-axis orientation perpendicular to \mathbf{H}_{FC} , in agreement with the above discussed sign of the AMR. Note that the comparison of measured AFM and ferromagnetic XMLD signals allowed us to confirm the spin-axis direction for the given direction of \mathbf{H}_{FC} provided that the sign of the XMLD signal is independent of whether the spin-axis direction corresponds to the AFM or ferromagnetically aligned Fe moments. This can be verified by the full-potential *ab initio* theory of XMLD spectra in transition-metal magnets³⁰. We performed the calculations and found, as expected, that the sign of the XMLD signal is the same for the AFM and ferromagnetic states of FeRh and that the overall XMLD spectra are almost identical for the two types of magnetic order.

Detailed structural and magnetic characterization

Having established the microscopic physical description of key functionalities of our AFM memory resistor we resume in the remaining paragraphs the more detailed description of our experimental findings. The high epitaxial quality of our FeRh films is illustrated in Fig. 2d–f. The cross-section of the FeRh thin film at the interface with the MgO substrate (Fig. 2d), viewed down the (112) and (100) zone axis of the two respective materials, shows that the FeRh epilayer is fully coherent with the MgO substrate. The micrograph demonstrates nearly perfect ordering of the atoms in the FeRh unit cell. X-ray diffraction patterns (Fig. 2e) show only the

{001} family of peaks of both FeRh and MgO, confirming that the samples are textured with no spurious phases. In Fig. 2f we show the wavelength dispersive X-ray spectroscopy analysis of the chemical composition of our FeRh film. We observe a small Fe deficit from the target's nominal 1:1 stoichiometry with Fe/Rh ≈ 0.94 –0.96.

Figure 3 presents magnetic characterization of our FeRh film by the superconducting quantum interference device and vibrating sample magnetometer, which provides further insight into the behaviour of our AFM memory. In Fig. 3a we show temperature-dependent magnetization data recorded at different magnetic fields. When warming up, the magnetization exhibits a clear signature of the transition from the AFM to the ferromagnetic phase of FeRh. The thermal hysteresis reflects the first-order nature of the transition⁴. When increasing the magnetic field, the ferromagnetic phase is stabilized and the transition occurs at lower temperatures. Note that at 400 K, a field of 9 T is strong enough to fully stabilize the ferromagnetic state. In our transport measurement set-up, the highest allowed temperature was 400 K, so we applied \mathbf{H}_{FC} of 9 T to safely enter the ferromagnetic state at this temperature. At lower temperatures, the system gradually turns into the AFM state. The XMLD experimental set-up allowed us to perform the field-cooling procedure from 500 K. In this case, \mathbf{H}_{FC} of 0.5 T was sufficient to stabilize the two orthogonal metastable spin axes configurations in the room-temperature AFM memory state.

Complementary magnetic-field-dependent magnetization traces are plotted in Fig. 3b,c. At 400 K, the data are consistent with the ferromagnetic alignment of Fe spins and identical signal is detected while sweeping the magnetic field along the [100] or [010] crystal directions (Fig. 3c). This confirms the expected in-plane cubic symmetry of our FeRh film deposited on the cubic MgO substrate. We note that the loops were obtained by sweeping the magnetic field between ± 9 and 400 K. Magnetization data measured at room temperature and 200 K (Fig. 3b) confirm the

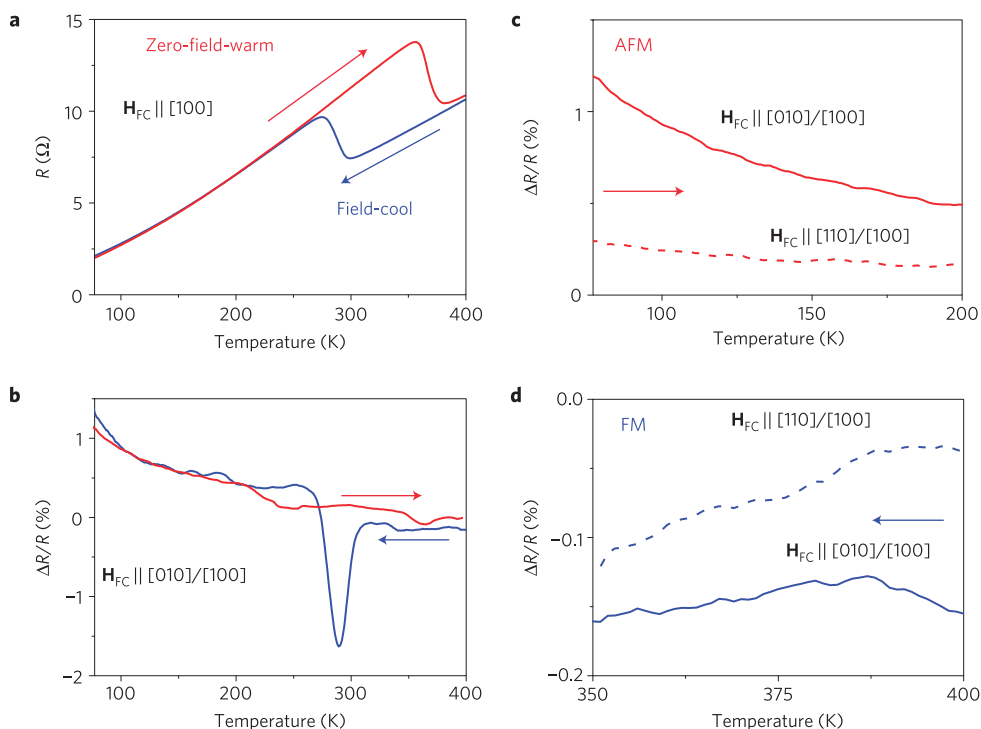


Figure 5 | Temperature dependence of the AMR. **a**, Resistance measured while field-cooling from 400 K in H_{FC} of 9 T \parallel [100] and while subsequently warming up in zero magnetic field. **b**, Relative resistance difference, $(R(H_{FC} \parallel [010]) - R(H_{FC} \parallel [100]))/R(H_{FC} \parallel [100])$, for the field-cool and zero-field-warm measurements. **c**, Low-temperature zero-field-warm relative resistance differences, $(R(H_{FC} \parallel [010]) - R(H_{FC} \parallel [100]))/R(H_{FC} \parallel [100])$ (solid line) and $(R(H_{FC} \parallel [110]) - R(H_{FC} \parallel [100]))/R(H_{FC} \parallel [100])$ (dashed line). **d**, High-temperature field-cool relative resistance differences, $(R(H_{FC} \parallel [010]) - R(H_{FC} \parallel [100]))/R(H_{FC} \parallel [100])$ (solid line) and $(R(H_{FC} \parallel [110]) - R(H_{FC} \parallel [100]))/R(H_{FC} \parallel [100])$ (dashed line).

AFM order. Only a very weak residual moment remains in the system, as seen from the minor hysteretic contribution to the signal at low (~ 100 mT) fields. Its origin can be associated with the small departure of our FeRh film from the nominal 1:1 stoichiometry of the fully compensated FeRh AFM (Fig. 2b) or with the presence of residual ferromagnetic regions in the AFM matrix as is common in first-order transitions. We ascribe the weak variation of the resistance seen in Fig. 1e in the field-rotation measurement to this residual moment. We point out, however, that the residual moment that is reversed at the low, ~ 100 mT field (Fig. 3b) cannot be responsible for the AMR signal distinguishing the two memory states because these distinct resistance states remain stable up to the largest field (9 T) applied in our experiments. The residual moment has also no marked effect on our AFM memory states as the difference between the corresponding resistances is much larger than the weak variations of the individual angular dependencies of each of the two memory states.

Magnetization data in Fig. 3a–c are further complemented by the temperature-dependent magnetotransport measurements shown in Fig. 3d. At 340 K, the moments are aligned in the large applied magnetic field, resulting in a negative and hysteretic magnetoresistance trace in the field-sweep measurement. Similar data are obtained at 320 K. However, the hysteretic field-dependent part of the resistance trace is shifted to higher magnetic fields as we move further away in temperature from the AFM–ferromagnetic transition. We note that these measurements are consistent with a recent study of similar FeRh/MgO samples that focused on magnetotransport effects near the AFM–ferromagnetic transition¹⁴. The aim of our paper is, however, to demonstrate the memory functionality and AMR in the AFM state below the transition. In particular, at room temperature and at 200 K we do not see any field

dependence of the resistance on the x – y -scale of Fig. 3d, confirming that the FeRh film behaves basically as a compensated AFM with a negligible residual moment at these low temperatures and up to the highest applied magnetic fields.

In Fig. 4 we inspect the 200 K and room-temperature resistance traces in the large field range and on a fine resistance scale, for the two memory states set up by the cooling-in-field procedures described in Fig. 1. At 200 K we observe a parabolic positive magnetoresistance that reaches $\sim 1\%$ at 9 T (Fig. 3a). We ascribe it to the ordinary, Lorentz force magnetoresistance that is independent of spin. Indeed, the two traces have just a constant offset; that is, cycling our AFM memory between ± 9 and 200 K has no effect on the stability of the two distinct AFM states. This is further confirmed in Fig. 4b where instead of sweeping the magnetic field we rotate the sample in a 9 T applied field. We observe small variations of the resistance, which we ascribed above to the residual uncompensated moments. However, as seen in Fig. 4b, the two distinct AFM memory states remain clearly separated even in the 9 T rotating field.

In Fig. 4c we plot room-temperature magnetoresistance traces on a similar fine scale and we observe a different behaviour in the strong magnetic fields than at 200 K. The ordinary spin-independent positive magnetoresistance is not visible because of a stronger hysteretic negative magnetoresistance. Compared with the traces at 320 and 340 K plotted in Fig. 3d, it is clear that this, relatively small hysteretic magnetoresistance seen at room temperature reflects that with increasing temperature and large field the system approaches the transition to the ferromagnetic coupling of spins. However, at room temperature and up to the highest applied magnetic field of 9 T the system remains far from the complete transition to the ferromagnetic order. As further highlighted in Fig. 4d, this implies that we can cycle our AFM FeRh memory between ± 9 T fields

at room temperature without disturbing either of the two distinct memory states.

Finally, in Fig. 5, we provide a more detailed investigation of the temperature dependence of the FeRh AMR spanning a broad temperature range from 400 to 77 K. To relate these measurements to the writing and reading methods demonstrated above for our FeRh AFM memory we show transport data acquired while cooling the sample in a magnetic field and, subsequently, by warming it in zero magnetic field. The temperature-dependent resistances are plotted in Fig. 5a. The resistance trace measured while cooling in an applied field (H_{FC} of 9 T \parallel [100]) shows the step corresponding to the ferromagnetic–AFM transition at a lower temperature than the resistance trace measured while subsequently warming the sample in a zero field, consistent with the measurements shown in Fig. 4. The relative difference between resistance traces for $H_{FC} \parallel$ [010] and [100] is plotted in Fig. 5b. On the low-temperature side below the ferromagnetic–AFM transition, the data correspond to the temperature-dependent AFM-AMR as defined in Fig. 1. As expected, the magnitude of the AMR increases when moving from the transition towards low temperatures and reaches the $\sim 1\%$ scale in agreement with our microscopic calculations. On the high-temperature side, we can use the measurements in applied magnetic field to assess the AMR in the ferromagnetic state. A detailed comparison of the AFM-AMR on the low-temperature side and the ferromagnetic-AMR on the high-temperature side is presented in Fig. 5c,d. Considering the relative angle of the spin axes and current, the measurements confirm that the AFM and ferromagnetic AMRs have the same sign because in the former case the spin axis aligns perpendicular to H_{FC} while in the latter case the spin axis (magnetization) is parallel to H_{FC} . In Fig. 5c,d we also show the relative difference between resistance traces for $H_{FC} \parallel$ [110] and [100]. Consistent with the AMR phenomenology, $H_{FC} \parallel$ [110] (45° from the current direction) produces an intermediate resistance state between the two extreme resistance states prepared by $H_{FC} \parallel$ [100] and $H_{FC} \parallel$ [010].

Discussion

We have demonstrated a room-temperature AFM memory and explained the AFM-AMR effect we employed for a simple ohmic resistance read-out. Our magnetic memory shows the unique features of AFMs. In particular, it is insensitive to strong magnetic field perturbations and produces negligible stray fields. The magnitude of the AFM-AMR effect in our FeRh sample is sufficient to reproducibly detect the two distinct memory states at room temperature.

Our work represents the proof of principle demonstration of an AFM memory resistor, yet there is much room for improving all of the functionalities of such a device. We note, however, that the magnetic memory concept we introduce is generic to a broad class of spin–orbit-coupled AFMs. Our microscopic calculations and temperature-dependent AFM-AMR measurements indicate a route for increasing the magnitude of the AFM-AMR in materials with higher transition temperatures. The same theory framework or measurements can systematically map ohmic AMRs in a variety of metallic AFMs. To improve our cooling-in-field procedure for writing, future studies of AFM memories can benefit from the extensive research and development of techniques in ferromagnets for heat-assisted magnetic recording³¹. In our FeRh samples, the temperature and field strength can still be optimized to achieve the most efficient writing in this material. Other systems that show the high-temperature AFM–ferromagnetic transition can be considered or, as recently demonstrated in a tunnelling IrMn device¹⁰, heating close to the AFM to paramagnetic transition in materials without the AFM–ferromagnetic transition point may be a viable alternative. A highly attractive approach for AFMs is to use spin–orbit coupling not only for reading but also for writing the state by electrical means.

This is a concept that in ferromagnets has recently drawn much attention from both fundamental physics and memory application perspectives^{32,33} but in AFMs is yet to be explored. As the effect of the spin-axis reorientation on electrical transport has been demonstrated in our work, the commonly observed reciprocity between spin and charge dynamics implies the possibility to generalize the ferromagnetic spin-torque phenomena³⁴ to AFMs. Beyond the electrical means, spins in magnetic materials can be reoriented optically, which in AFMs may provide for ultrafast, precession-free writing schemes³⁵.

Methods

Thin films were prepared by d.c. sputtering. MgO(001) substrates were heated up to 550 K in a base pressure of 10^{-8} torr. Subsequently, Ar gas was introduced (3 mtorr) and films were grown using 50 W power at a rate of 1 nm min^{-1} using a stoichiometric FeRh target.

X-ray diffraction experiments were carried out using a Panalytical X'Pert Pro diffractometer by Philips. The composition and thickness of the thin films were obtained by variable-voltage electron-probe microanalysis, using a CAMECA SX-50 electron microprobe equipped with four wavelength-dispersive X-ray spectrometers. X-ray intensities were measured at 10, 12, 15 and 20 keV electron incident energy and they were analysed with the help of the program STRATAGEM (SAMX), which calculates the thickness and composition of a multilayer target by least-squares fitting of an analytical X-ray emission model to the experimental data.

The cross-sectional sample for transmission electron microscopy was prepared by mechanical polishing followed by Ar ion milling. High-angle annular dark-field scanning transmission electron microscopy imaging was performed on an FEI titan, the TEAM0.5 at the National Center for Electron Microscopy. The image shown in Fig. 2a is an averaged region from a scanning transmission electron micrograph taken with a high-angle annular dark-field detector. This mode highlights the atom nucleus with intensity corresponding to the atomic number; here Rh ($Z = 45$) appears brightest followed by Fe ($Z = 26$), and Mg ($Z = 12$) in the substrate. The image was averaged laterally over approximately 30 adjacent unit cells.

Magnetic characterization with magnetic fields up to 5 T was carried out in a superconducting quantum interference device by Quantum Design using the Reciprocating Sample Option. Measurements up to 9 T were performed in a vibrating sample magnetometer by Quantum Design.

Fe L-edge XMLD measurements were performed at Beamline 4.0.2 of the Advanced Light Source. Field-cooling was performed from 500 K with the largest magnetic field of 0.5 T allowed by the XMLD measurement set-up.

Transport experiments were four-probe resistance measurements carried out using the Physical Property Measurement System by Quantum Design in resistivity mode and equipped with a horizontal rotator module. For parallel current (bi-polar constant current ranging from 1 to $10 \mu\text{A}$) and magnetic field position θ is defined as 0, along the substrate [100] direction shown. Maximum magnetic field and temperature allowed by the transport measurement set-up are 9 T and 400 K, respectively.

Kubo formula CPA-TB-LMTO calculations were performed for the cubic, CsCl crystal structure of FeRh. The structure of the AFM state was described as a stacking of four interpenetrating face-centred-cubic sublattices along the [111]-direction occupied respectively by Fe[up], Rh, Fe[down] and Rh atoms. Substitutional Rh_{Fe} disorder was placed on both Fe sublattices in the considered Rh-rich ($Fe_{1-x}Rh_x$)Rh random alloy. The model of quasiparticle broadening was treated by adding a constant, spin-independent imaginary part of the self-energy (of order 10^{-3} – 10^{-2} Ry). A large number ($\sim 10^7$) of points in the full face-centred-cubic Brillouin zone was used to obtain converged AMR values.

Received 7 August 2013; accepted 10 December 2013;
published online 26 January 2014

References

- Umetsu, R. Y., Sakuma, A. & Fukamichi, K. Magnetic anisotropy energy of antiferromagnetic L10-type equiatomic Mn alloys. *Appl. Phys. Lett.* **89**, 052504 (2006).
- Szunyogh, L., Lazarovits, B., Udvardi, L., Jackson, J. & Nowak, U. Giant magnetic anisotropy of the bulk antiferromagnets IrMn and IrMn₃ from first principles. *Phys. Rev. B* **79**, 020403 (2009).
- Thomson, W. On the electro-dynamic qualities of metals: Effects of magnetization on the electric conductivity of nickel and of iron. *Proc. R. Soc. Lond.* **8**, 546–550 (1857).
- McGuire, T. & Potter, R. Anisotropic magnetoresistance in ferromagnetic 3d alloys. *IEEE Trans. Magn.* **11**, 1018–1038 (1975).
- Shick, A. B., Khmelevskiy, S., Mryasov, O. N., Wunderlich, J. & Jungwirth, T. Spin-orbit coupling induced anisotropy effects in bimetallic antiferromagnets: A route towards antiferro-magnetic spintronics. *Phys. Rev. B* **81**, 212409 (2010).

6. Park, B. G. *et al.* A spin-valve-like magnetoresistance of an antiferromagnet-based tunnel junction. *Nature Mater.* **10**, 347–351 (2011).
7. Duine, R. Spintronics: An alternating alternative. *Nature Mater.* **10**, 345 (2011).
8. Marti, X. *et al.* Electrical measurement of antiferromagnetic moments in exchange-coupled IrMn/NiFe stacks. *Phys. Rev. Lett.* **108**, 017201 (2012).
9. Wang, Y. Y. *et al.* Room-temperature perpendicular exchange coupling and tunneling anisotropic magnetoresistance in an antiferromagnet-based tunnel junction. *Phys. Rev. Lett.* **109**, 137201 (2012).
10. Petti, D. *et al.* Storing magnetic information in IrMn/MgO/Ta tunnel junctions via field-cooling. *Appl. Phys. Lett.* **102**, 192404 (2013).
11. Marder, M. P. *Condensed Matter Physics* (Wiley, 2000).
12. Loh, S., Baumann, S., Lutz, C. P., Eigler, D. M. & Heinrich, A. J. Bistability in atomic-scale antiferromagnets. *Science* **335**, 196–199 (2012).
13. Shirane, G., Chen, C. W., Flinn, P. A. & Nathans, R. Mossbauer study of hyperfine fields and isomer shifts in the Fe–Rh alloys. *Phys. Rev.* **131**, 183–190 (1963).
14. Sharma, M. *et al.* Magnetotransport properties of epitaxial MgO(001)/FeRh films across the antiferromagnet to ferromagnet transition. *J. Appl. Phys.* **109**, 083913 (2011).
15. Mariager, S. O., Guyader, L. L., Buzzi, M., Ingold, G. & Quitmann, C. Imaging the antiferro-magnetic to ferromagnetic first order phase transition of FeRh. Preprint at <http://arxiv.org/abs/1301.4164>.
16. Banhart, J. & Ebert, H. First-principles theory of spontaneous-resistance anisotropy and spontaneous Hall effect in disordered ferromagnetic alloys. *Europhys. Lett.* **32**, 517–522 (1995).
17. Ebert, H., Vernes, A. & Banhart, J. Anisotropic electrical resistivity of ferromagnetic Co–Pd and Co–Pt alloys. *Phys. Rev. B* **54**, 8479–8486 (1996).
18. Vernes, A., Ebert, H. & Banhart, J. Electronic conductivity in NiCr and NiCu fcc alloy systems. *Phys. Rev. B* **68**, 134404 (2003).
19. Turek, I. & Zalezak, T. Residual resistivity and its anisotropy in random CoNi and CuNi ferromagnetic alloys. *J. Phys. Conf. Ser.* **200**, 052029 (2010).
20. Turek, I., Kudrnovský, J. & Drchal, V. *Ab initio* theory of galvanomagnetic phenomena in ferromagnetic metals and disordered alloys. *Phys. Rev. B* **86**, 014405 (2012).
21. Gould, C. *et al.* Tunneling anisotropic magnetoresistance: A spin-valve like tunnel magnetoresistance using a single magnetic layer. *Phys. Rev. Lett.* **93**, 117203 (2004).
22. Brey, L., Tejedor, C. & Fernández-Rossier, J. Tunnel magneto-resistance in GaMnAs: Going beyond Jullière formula. *Appl. Phys. Lett.* **85**, 1996–1998 (2004).
23. Shick, A. B., Máca, F., Mašek, J. & Jungwirth, T. Prospect for room temperature tunnelling anisotropic magnetoresistance effect: Density of states anisotropies in CoPt systems. *Phys. Rev. B* **73**, 024418 (2006).
24. Gao, L. *et al.* Bias voltage dependence of tunneling anisotropic magnetoresistance in magnetic tunnel junctions with MgO and Al₂O₃ tunnel barriers. *Phys. Rev. Lett.* **99**, 226602 (2007).
25. Moser, J. *et al.* Tunneling anisotropic magnetoresistance and spin-orbit coupling in Fe/GaAs/Au tunnel junctions. *Phys. Rev. Lett.* **100**, 056601 (2007).
26. Park, B. G. *et al.* Tunneling anisotropic magnetoresistance in multilayer-(Co/Pt)/AlO_x/Pt structures. *Phys. Rev. Lett.* **100**, 087204 (2008).
27. Marti, X. *et al.* Anisotropic magnetoresistance in antiferromagnetic semiconductor Sr₂IrO₄ epitaxial heterostructure. Preprint at <http://arxiv.org/abs/1303.4704>.
28. Rushforth, A. W. *et al.* Anisotropic magnetoresistance components in (Ga,Mn)As. *Phys. Rev. Lett.* **99**, 147207 (2007).
29. Stöhr, J., Padmore, H. A., Anders, S., Stammer, T. & Scheinfein, M. R. Principles of X-ray magnetic dichroism spectromicroscopy. *Surf. Rev. Lett.* **5**, 1297–1308 (1998).
30. Kuneš, J. & Oppeneer, P. M. Anisotropic x-ray magnetic linear dichroism at the L edges of cubic Fe, Co, and Ni: *Ab initio* calculations and model theory. *Phys. Rev. B* **67**, 024431 (2003).
31. Chappert, C., Fert, A. & Dau, F. N. V. The emergence of spin electronics in data storage. *Nature Mater.* **6**, 813–823 (2007).
32. Miron, I. M. *et al.* Perpendicular switching of a single ferromagnetic layer induced by in-plane current injection. *Nature* **476**, 189 (2011).
33. Liu, L. *et al.* Spin-torque switching with the giant spin hall effect of tantalum. *Science* **336**, 555–558 (2012).
34. Kurebayashi, H. *et al.* Observation of a Berry phase anti-damping spin-orbit torque. Preprint at <http://arxiv.org/abs/1306.1893>.
35. Kimel, A. V., Kirilyuk, A., Tsvetkov, A., Pisarev, R. V. & Rasing, Th. Laser-induced ultrafast spin reorientation in the antiferromagnet TmFeO₃. *Nature* **429**, 850–853 (2004).

Acknowledgements

The authors acknowledge the support from the NSF (Nanosystems Engineering Research Center for Translational Applications of Nanoscale Multiferroic Systems, Cooperative Agreement Award EEC-1160504) and DOE. Transmission electron microscopy characterization was performed at NCEM, which is supported by the Office of Science, Office of Basic Energy Sciences of the US Department of Energy under Contract No. DE-AC02-05CH11231. J.F. acknowledges financial support from the Spanish Government (Projects MAT2011-29269-C03, CSD2007-00041) and Generalitat de Catalunya (2009 SGR 00376); C.F. acknowledges financial support from the Spanish Government (Projects MAT2012-33207, CSD2007-00041). I.F. acknowledges a Beatriu de Pinós postdoctoral scholarship (2011 BP-A 00220) and the Catalan Agency for Management of University and Research Grants (AGAUR-Generalitat de Catalunya). X.M. acknowledges the Grant Agency of the Czech Republic No. P204/11/P339. Research at the University of Nottingham was funded by EPSRC grant EP/K027808/1. T.J. acknowledges support from the ERC Advanced Grant 268066, Praemium Academiae of the Academy of Sciences of the Czech Republic, and from the Ministry of Education of the Czech Republic Grant LM2011026. S.S. acknowledges funding by STARnet FAME. J. Kuneš 83 and I.T. acknowledge the Czech Science Foundation No. P204/11/1228.

Author contributions

Sample preparation, R.J.P., J.D.C., L.Y.; scanning transmission electron microscopy, C.T.N.; magnetotransport and structural characterization, I.F. and C.F.; data analysis, I.F., C.F., P.W., J.-H.C. and D.Y.; X-ray linear dichroism, J.L., E.A. and Q.H.; theory, J. Kudrnovský, I.T. and J. Kuneš; writing and project planning, X.M., T.J., J.F., P.W., S.S. and R.R.

Additional information

Reprints and permissions information is available online at www.nature.com/reprints. Correspondence and requests for materials should be addressed to X.M.

Competing financial interests

The authors declare no competing financial interests.